Improving spike separation using waveform derivatives

Zhi Yang, Qi Zhao and Wentai Liu

School of Engineering, University of California at Santa Cruz, 1156 High Street, Santa Cruz,
CA 95064, USA

E-mail: yangzhi@soe.ucsc.edu, zhaoqi@soe.ucsc.edu and wentai@soe.ucsc.edu

Abstract
This paper presents spike derivatives as a tool for spike feature extraction to improve the
separation of similar neurons. The theoretical framework of neuronal geometry signatures and
noise shaping to perform the spike derivative is formulated first, and based on the derivations
we show that the first derivative of the spikes manifests the waveform difference contributed
by the geometry signatures and also reduces the associated low-frequency noise. Quantitative
comparisons of sorting neurons using spikes and their derivatives are performed on spike
sequences from a public database, and improved results are observed when using spike
derivatives.

(Some figures in this article are in colour only in the electronic version)

1. Introduction

Neurons communicate by firing action potentials, which
induce transient voltage fluctuations in the surrounding neural
tissues. The voltage fluctuations can be recorded with
extracellular electrodes, where the signals take the shape of
spikes. A recording electrode is often surrounded by multiple
firing neurons, causing the recorded activities to become
superimposed. To extract and understand signal processing
in a biological neural network, the spikes must be resolved
into individual neuronal sources [1–6]. This labeling process
is called spike sorting.

Sorting neural spikes is challenging due to several
factors, such as the presence of unresolved neuronal activity,
similarity in recorded shapes and magnitudes of firing neurons,
overlapping of spikes from simultaneously firing neurons,
as well as changes in signal amplitude obtained from the
same neuron at different times [1, 7–9]. If the sorting
algorithm fails to differentiate signals from similar neurons,
it will inaccurately report one frequently firing neuron,
which compromises the reliability and accuracy of the neural
information decoder.

Commonly used spike feature extraction algorithms
include principal component analysis (PCA) [10, 11],
the Bayesian algorithm [12], template matching [13–16],
wavelets [17–19], independent component analysis (ICA)
[20–24] and inter-spike interval based algorithms [18, 25–27].
The performance of the feature extraction algorithms
in differentiating similar neurons can be improved by
advanced training algorithms [13, 28–30], which are usually
computationally intensive, thus slowing down the training
process. Retraining is required when the electrodes move,
which could be frequent in certain applications [31, 32].
Although an early study has shown that computation of the
training algorithm is affordable, it was assumed that retraining
was performed daily [10]. For frequent retraining in a shorter
period, as suggested in [31, 32], the implementation of a
complex training algorithm for a large number of channels
becomes more difficult in terms of computation.

This paper reports a method of using the first-order
derivative of spikes for the sorting of similar neurons.
The theoretical framework includes neuronal geometry
signatures and noise shaping. By evaluating neuronal
geometry signatures with the compartment model, we find
that emphasizing a high-frequency signal spectrum helps
differentiate similar neurons. Because the associated spike
noise is dominant at a lower-frequency spectrum, a frequency
shaping filter could be used to reduce the noise. The operation
of the derivative is a simple frequency shaping filter that
almost linearly emphasizes the signal spectrum according
to the frequency. Combining the spike derivative and a
conventional spike feature extraction algorithm, improved

separation of similar neurons is achieved without complex training procedures.

The rest of the paper is organized as follows. Section 2 introduces the theoretical framework. Section 3 presents sorting procedures and experimental results. Section 4 summarizes the work.

2. Theory

2.1. Geometry signatures of similar neurons

This section focuses on the derivations of neuronal geometry signatures, which are used for sorting similar neurons. If the transmembrane current profiles from all membrane segments are obtained, the potential around the target neuron can be modeled by Laplace's equation [33]:

$$\nabla^2 V = 0, \tag{1}$$

with the boundary condition $V = 0$ at infinity and

$$\sigma_e \nabla V \cdot \overrightarrow{n} = j_m, \tag{2}$$

where j_m is the transmembrane current, σ_e is the conductivity, and $\overrightarrow{n}$ is the normal to the cell membrane. The induced voltage waveform is

$$V(\overrightarrow{r_0}, t) = \int \frac{j_m(\overrightarrow{r}, t)\, \mathrm{d}r}{4\pi\sigma_e |\overrightarrow{r} - \overrightarrow{r_0}|}, \tag{3}$$

where $\overrightarrow{r_0}$ denotes the location of the electrode, and $\overrightarrow{r}$ describes the locations of the active membranes.

Since action potentials propagate slowly along the axonal branches of the cortical neurons (e.g., an average of 0.5––2 m s^{-1} for hippocampal neurons [34]), the recorded active membranes usually do not fire simultaneously. As a result, the detailed geometry of the underlying neuron influences the shape of the spikes. Following the computational model described in [35–38], a neuron is modeled as compartment elements including soma, axon hillock and axonal branches. Different compartment elements may have different ion channel densities, resulting in different transmembrane current profiles. An extracellular electrode only records those membrane segments within the recording radius, which is measured to be tens of μm [39]. Meanwhile, many cortical neurons have axonal branches up to hundreds of μm or more [34, 40–42], and membranes within the recording radius are simply modeled as one or a few compartments with uniform ion channel densities. As a result, the spike waveform can be expressed as the convolution of the transmembrane current profile and an implicit geometry kernel function:

$$V(t) = \int j_m(\tau) W(t - \tau)\, \mathrm{d}\tau, \tag{4}$$

where $W(t)$ is the geometry kernel function determined by geometry properties of the recorded membrane segments, and the integration range is from $-\infty$ to ∞. From here on, this integration range is used as the default if not specified.

It is possible that the recorded neurons have distinguished spikes, which can easily be captured by a sorting algorithm. It is also possible that the recorded neurons have similar shaped spikes, due to similar ion channel densities. However, as shown in figure 1, if the magnitudes of such spikes are also similar, the separation becomes challenging. A general spike sorting algorithm, without complex training procedures, may fail to resolve such ambiguity and will inaccurately report a single, large, spike cluster, which affects the reliability and accuracy of the decoder. The approach of differentiating the associated kernel functions could be used to sort similar spikes. Assume $W_1(t)$ and $W_2(t)$ are the geometry kernel functions of two neurons with the same ion channel population; the difference between the two spikes is

$$\triangle V(t) = \int j_m(\tau)[W_1(t - \tau) - W_2(t - \tau)]\, \mathrm{d}\tau. \tag{5}$$

Although it is tempting to extract the shape, width and magnitude of the kernel function to sort spikes, the approach is not practical due to the unknown transmembrane current profile j_m. A spectrum evaluation of $W(t)$, however, offers certain useful information that may help waveform separation. Using the recording radius (50 μm [39]) to approximate the action potential propagation length within the recording range, 0.5–2 m s^{-1} [34] as the propagation speed, the width of the kernel function is roughly estimated as the ratio of the action potential propagation length divided by the propagation speed. Therefore, in the frequency domain, $W(t)$ exhibits a wider spectrum as compared with spikes (from several hundreds μs up to a few ms in width). This result is consistent with simplified neuron spike models that use a simple treatment of approximating $W(t)$ as a delta function, $\delta_i(t)$:

$$\delta_i(t) = \begin{cases} 0 & t \neq 0 \\ i & t = 0. \end{cases} \tag{6}$$

For waveforms that cannot be differentiated under simplified spike models, e.g., satisfying $\int (W_1(t) - W_2(t))\, \mathrm{d}t \approx 0$, the shape, width and magnitude of the kernel function can contribute to deviations at higher-frequency points, as illustrated in figure 2. To differentiate the waveforms, we rewrite equation (5) in the frequency domain as

$$\mathcal{F}(\triangle V) = \mathcal{F}(j_m)\mathcal{F}(W_1 - W_2), \tag{7}$$

where $\mathcal{F}(\cdot)$ denotes the Fourier transform. The condition of $\int [W_1(t) - W_2(t)]\, \mathrm{d}t \approx 0$ is equivalent to $\mathcal{F}(W_1 - W_2) \approx 0|_{f=0\,\mathrm{Hz}}$, which implies that the waveform difference caused by the geometry kernel functions has a smaller contribution at a lower-frequency spectrum. A more quantitative explanation can be given by studying the derivative of $\mathcal{F}(\triangle V)$ with respect to the frequency using equation (7):

$$\frac{\partial \mathcal{F}(\triangle V)}{\partial f} = \frac{\partial \mathcal{F}(j_m)}{\partial f}\mathcal{F}(W_1 - W_2) + \mathcal{F}(j_m)\frac{\partial \mathcal{F}(W_1 - W_2)}{\partial f}, \tag{8}$$

where f is the frequency.

Note that $\mathcal{F}(j_m)$ is a band-limited signal, and $\mathcal{F}(W_1 - W_2)$ serves as a notch frequency mask with a relatively wider spectrum. The first term in equation (8) is attenuated by $\mathcal{F}(W_1 - W_2)$ within the dominant spectrum of $\mathcal{F}(j_m)$. Otherwise, an appreciable waveform difference is expected according to equation (7).
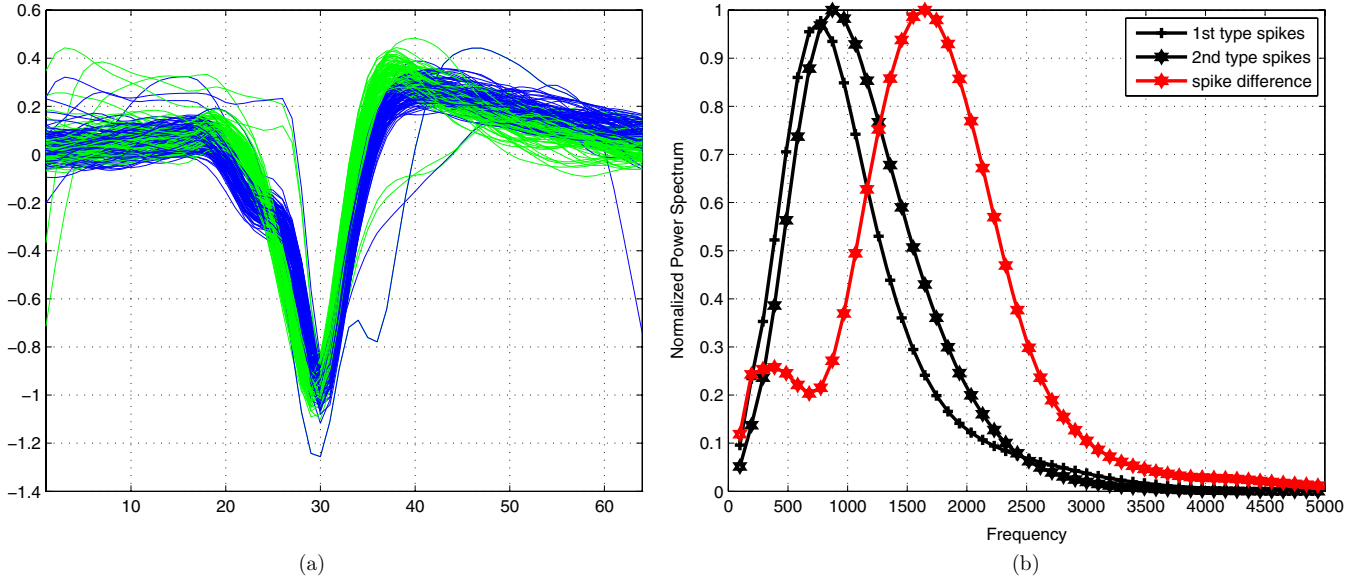
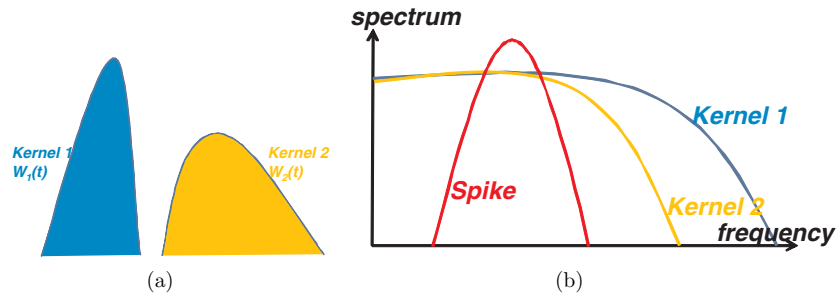**Figure 1.** (a) Superimposed spikes from two neurons. (b) Estimated spectrum of spikes and their difference.

Figure 2. (a) Kernel function illustrations in the time domain that satisfies $\int [W_1(t) - W_2(t)] \, dt \approx 0$. (b) Illustrations of kernel functions and a spike in the frequency domain.

The second term in equation (8), on the other hand, exhibits a strong frequency dependence within the dominant spectrum of $\mathcal{F}(j_m)$. It can be expanded as

$$\mathcal{F}(j_m) \frac{\partial \mathcal{F}(W_1 - W_2)}{\partial f}$$

$$= -j2\pi \mathcal{F}(j_m) \int [W_1(t) - W_2(t)] t \, e^{-2\pi jft} \, dt$$

$$\approx 2\pi \mathcal{F}(j_m) \int (W_1(t) - W_2(t)) t \sin(2\pi ft) \, dt, \quad (9)$$

where the approximation holds when kernel functions W_i are symmetrical.

As a summary, the waveform difference between similar neurons caused by geometry functions satisfies the following conditions:

$$\begin{cases} \mathcal{F}(\triangle V) \approx 0 \big|_{f=0\,\text{Hz}} \\ \dfrac{\partial \mathcal{F}(\triangle V)}{\partial f} \approx f 4\pi^2 \mathcal{F}(j_m) \int (W_1(t) - W_2(t)) \\ \qquad \times t^2 \dfrac{\sin(2\pi ft)}{2\pi ft} \, dt \propto f. \end{cases} \quad (10)$$

In equation (10), $\frac{\partial \mathcal{F}(\triangle V)}{\partial f}$ is linear to frequency f at a low-frequency region, as $\frac{\sin(2\pi ft)}{2\pi ft} \approx 1$. The amplification by a

factor of f leads to a higher-frequency spectrum of $\mathcal{F}(\triangle V)$. As a result, a frequency shaping filter with an emphasis on a high-frequency spectrum may help differentiate kernel functions.

The frequency shaping filter also modifies the spectrum of noise; a further improved waveform separation can be achieved if it reduces the noise. A detailed analysis on noise is shown in section 2.2.

2.2. The frequency shaping filter and the spike derivative

In section 2.1, we discussed the separation of similar neurons using a frequency shaping filter with an emphasis on the high-frequency signal spectrum without considering the noise. The noise power spectrum, however, is clearly modified by the frequency shaping filter. Intuitively, low-frequency noise is reduced, and high-frequency thermal noise is amplified. In general, the power spectrum of the input referred noise at the first stage amplifier exhibits a decaying profile [43–45] and approximates as

$$N(f) = N_{\text{neu}} + N_{\text{e.e}} + N_{1/f} + N_{\text{therm}}$$

$$\approx N_{f_{c1}} \left(\frac{f_{c1}}{f} \right)^\alpha + N_{\text{therm}}, \quad (11)$$
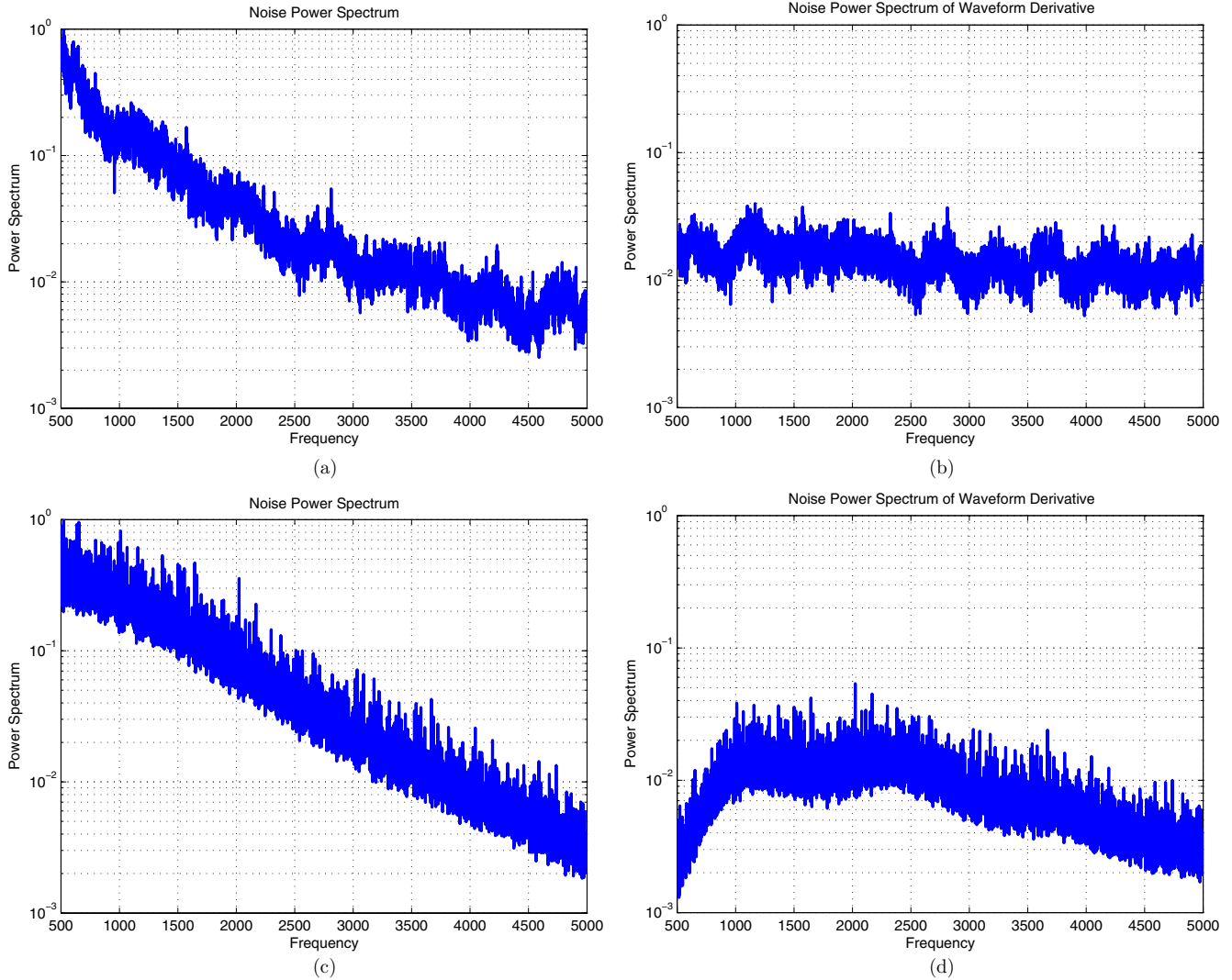
Figure 3. Noise properties of recordings from two preparations (500 Hz to 5 kHz). (a) Noise power spectrum measured from a cat. (b) Noise power spectrum of the derivative (the same data in (a) are used). (c) Noise power spectrum measured from a monkey. (d) Noise power spectrum of the derivative (the same data in (c) are used).

where N_{neu} is the neuronal noise, $N_{\text{e.e}}$ is the electrode–electrolyte interface noise, $N_{1/f}$ is the flicker noise, N_{therm} is the thermal noise contributed by tissue impedance and transistors, f_{c1} is the high-pass corner frequency of the digital filter, and $N_{f_{c1}}$ is the low-frequency noise at the frequency f_{c1}. Except thermal noise, the remaining noises are featured at low frequency and assumed to have a profile following $f^{-\alpha}$. Noise profile varies between both preparations and recording systems. Low-frequency noise, however, is typically dominant. As shown in figure 3, the noise power spectra recorded from two preparations are plotted. Within the signal band (hundreds of Hz to several kHz), a $f^{-\alpha}$ noise profile is observed.

Among various frequency shaping filters, taking a derivative is a simple one, which almost linearly emphasizes the signal spectrum according to frequency. For a discrete time spike sequence, taking the derivative after the analog-to-digital converter (ADC) has the frequency response of

$$H(f) = 2\,\mathrm{e}^{j\pi f/2}\sin(\pi f/f_s), \qquad (12)$$

where f_s is the sampling frequency of the ADC.

The effect of a frequency shaping filter on noise can be quantitatively evaluated by the expression

$$k = \frac{1}{N_0|H(f_{\text{spike}})|^2}\int_{f_{c1}}^{f_{c2}} N(f)|H(f)|^2\,\mathrm{d}f, \qquad (13)$$

where f_{ci} are the corner frequencies (3 dB attenuation frequency points) of the digital filter before feature extraction, f_{spike} is the center frequency of the spike signal, $N(f)$ is the estimated power spectrum of the noise, and N_0 is the integrated noise over passing band. If k is less than 1, the signal-to-noise ratio (SNR) further increases, which improves waveform separation.

After taking derivatives, the noise spectrum density changes to

$$N(f)|H(f)|^2 = 2\big[N_{f_{c1}}(f_{c1}/f)^{\alpha} + N_{\text{therm}}\big]\sin^2(\pi f/f_s). \quad (14)$$

For integer α, a closed-loop expression of the integrated noise after derivation (N_1) can be obtained from equation (14). With a further assumption that the sampling frequency is sufficiently higher than the signal spectrum, the

expression of N_1 could be generalized to the non-integer α as

$$N_1 \approx \frac{2N_{f_{c1}} f_{c1} \alpha \pi^2}{(3-\alpha) f_s^2} \left[f_{c2}^{3-\alpha} - f_{c1}^{3-\alpha} \right] + \frac{2N_{therm} \pi^2}{3 f_s^2} \left[f_{c2}^3 - f_{c1}^3 \right]. \tag{15}$$

Combining equations (13) and (15), the parameter k that is used to quantify the modification to SNR due to the frequency shaping filter is

$$k = \frac{\frac{N_{f_{c1}} f_{c1}^\alpha}{3-\alpha} \left(f_{c2}^{3-\alpha} - f_{c1}^{3-\alpha} \right) + \frac{N_{therm}}{3} \left(f_{c2}^3 - f_{c1}^3 \right)}{N_{f_{c1}} \frac{f_{c1}^\alpha}{1-\alpha} \left(f_{c2}^{1-\alpha} - f_{c1}^{1-\alpha} \right) + N_{therm} (f_{c2} - f_{c1})} \frac{1}{2 f_{spike}^2}. \tag{16}$$

The quantitative impact of the frequency shaping filter on noise is affected by the recording system and biological environment, and the typical values of α we observe vary around 2 within the signal band as shown in figure 3. Here, we use $\alpha = 2$ to illustrate the analysis:

$$k = \frac{N_{f_{c1}} f_{c1}^2 (f_{c2} - f_{c1}) + \frac{N_{therm}}{3} \left(f_{c2}^3 - f_{c1}^3 \right)}{N_{f_{c1}} f_{c1}^2 \left(\frac{1}{f_{c1}} - \frac{1}{f_{c2}} \right) + N_{therm} (f_{c2} - f_{c1})} \frac{f_{c2}^2}{2 f_{spike}^2}$$

$$\approx \frac{\frac{f_x^2}{f_{c2}} + \frac{f_{c2}}{3}}{\frac{f_x^2}{f_{c1}} + f_{c2}} \frac{f_{c2}^2}{2 f_{spike}^2} \tag{17}$$

with

$$f_x = f_{c1} \left(\frac{N_{f_{c1}}}{N_{therm}} \right)^{1/2}, \tag{18}$$

where f_x is the frequency at which the noise spectrum approximately settles to the thermal noise floor. During the measurement, f_x depends on the recording system and biological environment (varying from 6 to 12 kHz in measurement).

In the case that the digital filter's low-pass corner frequency f_{c2} is designed smaller or comparable to f_x, equation (17) can be simplified as

$$k \approx \frac{f_{c1} f_{c2}}{2 f_{spike}^2} \approx \frac{2 f_{c1} f_{c2}}{(f_{c1} + f_{c2})^2} \leqslant \frac{1}{2}, \tag{19}$$

where the approximation holds well if the center frequency of the spike signal is close to the middle point of the filter's passing band.

As a summary, the spectrum of the recorded noise exhibits a decaying profile with respect to the frequency within the signal band. Therefore, an appropriate frequency shaping filter could be used to further improve the SNR.

3. Spike sorting methods and results

Quantitative and comparative sorting experiments are carried out to demonstrate the usefulness of frequency shaping filters. The sorting procedures and results are described in this section.
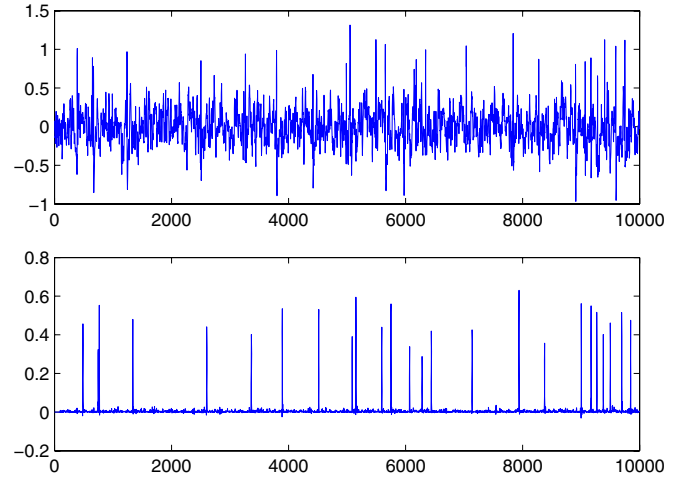

Figure 4. The upper trace is the digitized neural signal. The bottom trace is the NEO's output.

3.1. Spike detection

In this work, spikes are detected with the nonlinear energy operator (NEO) [46–49]. The NEO was formulated by Kaiser and is used for amplitude and frequency demodulation and speech analysis. It is also effective in detecting spikes that have localized high frequency and instantaneous energy. With a discrete time signal, the NEO is

$$\psi(V(n)) = V^2(n) - V(n+1)V(n-1). \tag{20}$$

A typical processing result using the NEO is illustrated in figure 4, where the upper trace is the raw neural signal and the bottom trace is the NEO's output. When high-frequency spike activity is present, the NEO generates a larger score.

Due to the improved separation of spike events (instantaneous high-energy events) and background activities (a mixture of low-frequency noise and thermal noise) using the NEO, the detection threshold becomes a less-sensitive parameter, which is shown by the receiver operating characteristic (ROC) curves in section 3.4. In this study, the threshold is set at three times the averaged energy score corresponding to 1.4% error detection and identifying 99.5% spikes as a worst case in this data set. A more detailed description is shown in section 3.4.

3.2. Spike feature extraction

Two commonly used spike feature extraction algorithms, including PCA [10, 11] and spike peaks [50], are applied to demonstrate the improved sorting results using the first derivative of spike waveforms.

All the algorithms are tested without performing interpolation. To quantify the performance of the feature extraction algorithms alone, spikes detected with small intervals are treated as overlapping events and ignored. In this paper, the minimal spike interval is set to be 1.2 ms, which could generally represent well-isolated individual spike events. A Bessel-type digital filter is applied to the identified spike waveforms before feature extraction. The corner frequencies (3 dB attenuation frequency point) of the filter are set to 250 Hz
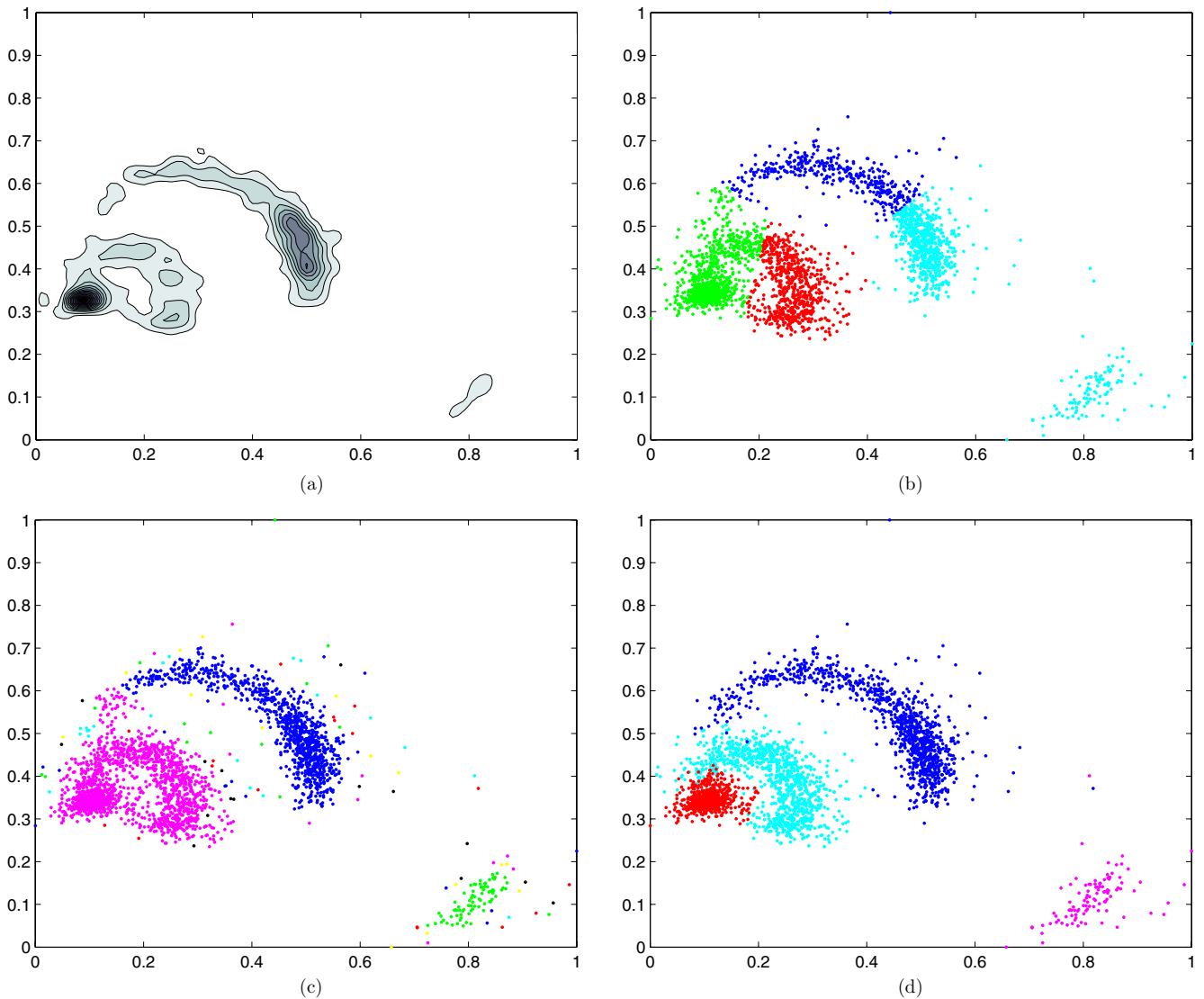
Figure 5. Comparative clustering results. (a) Contour lines of the spike feature map. (b) *k*-means clustering result with a four-cluster configuration. (c) Single linkage hierarchical clustering result with an over-specified (50) partitions. (d) Modified mean shift clustering result with a manually specified kernel scope.

and 6 kHz with 60 dB out-of-band rejection. With PCA-based feature extraction, the first two scores with the largest variance are used as the features. Compared with the feature extraction algorithm using spike peaks [50], a sample set including peaks of the spike derivative and spike height is used as counterpart features [44].

3.3. Spike clustering

An example of extracted spike features is shown in figure 5. This example illustrates several challenges faced by a spike clustering algorithm. First, the shapes of the clusters can be irregular and unpredictable. Second, the density and size of each cluster vary significantly. Third, the amount of data obtained is limited due to the acquisition and processing overhead. To overcome these challenges, we use the evolving mean shift clustering algorithm [51] to classify spikes. The algorithm converges data points to isolated modes, and points converging to the same mode are attributed to the same cluster.

The original mean shift algorithm is sensitive to the choice of the kernel radius [52–54]. Adaptive kernel radius estimation is reported in [55], which alleviates the problem to a certain extent. In this paper, the technique of adaptive kernel radius is applied, and the radius is chosen to be small. A side effect is that the algorithm tends to over-partition the data set into many sub-clusters, which is handled by a post-merging process. In the implementation, sub-clusters are merged based on two criteria. First, any modes with spike events less than 1% are forced to merge to their nearest modes. Second, sub-clusters are merged based on the density estimate at the boundary.

3.4. Similarity/dissimilarity measure of neural spikes

After the spikes have been sorted, it is desirable to have a similarity measure based on which the isolation quality of spike clusters can be quantitatively evaluated.

Similarity measures between distributions broadly fall into two categories: the bin-by-bin similarity measures
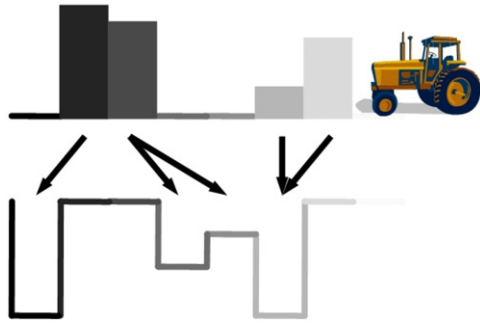
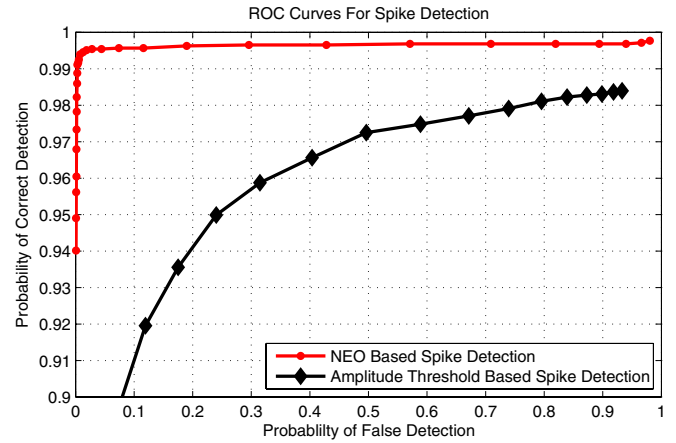**Figure 6.** Illustration of the earth mover's distance.

Figure 7. ROC curves for spike detection algorithms. The red-dotted curve is the result from NEO-based spike detection. The black-diamond curve is the result from amplitude-based spike detection

[56, 57] that only compare contents of the corresponding bins and the cross-bin similarity measures [58, 59] that also compare the non-corresponding bins. A noticeable property of recorded spikes is that there usually exists a significant amount of sample distortion [45] or misalignment due to the difficulty of synchronizing the sampling clock of ADC with the neurons' random activation. As a result, bin-by-bin distance measures, e.g., Euclidean distance measure, Bhattacharyya distance measure, are theoretically not preferable candidates for this application.

As a cross-bin similarity measure, which can be robust to waveform misalignment, the earth mover's distance (EMD) [60] gains its name from the intuition that given two waveforms, one can be seen as a mass of earth properly spread in space, the other as a collection of holes in that same space. As shown in figure 6, the EMD measures the least amount of work needed to fill all of the holes with all of the earth, where a unit of work corresponds to transporting a unit of earth by a unit of ground distance. In this paper, we formulate the EMD in the specific context of spike sorting, where the EMD is employed to compare a spike template (object model) and a spike waveform (object candidate). Specifically, we denote the ground distance between the uth sample in the object model and the vth sample in the object candidate as d_{uv} (e.g. Euclidean distance $d_{uv} = |u - v|$), and the flow (amount of transported earth) between them as f_{uv}. The goal is to find the smallest EMD and the best alignment t:

$$\arg \min_t (\min_{f_{uv}} Z(f_{uv}(t))). \tag{21}$$

In equation (21), the inner optimization is to find the EMD for each alignment, and the outer one is to obtain the best alignment. In the following, we use the superscript M to denote the object model and C for the object candidate. $w_u^{(M)}$ is the weight of the uth sample in the object model, and $w_v^{(C)}$ is the weight of the vth sample in the object candidate. As EMD works most conveniently on waveforms with non-negative, equally summed weights ($w_v^{(C)}$ and $w_u^{(M)}$), both the object candidate and the object model are vertically aligned to the same dc level with all the samples being positive:

$$w_i(n) = V_{\text{spike}}(n) - \frac{1}{N_{\text{spike}}} \sum_{n=1}^{N_{\text{spike}}} V_{\text{spike}}(n) + V_{\text{dc}}, \tag{22}$$

where w_i represents an object candidate/model, V_{spike} represents a spike waveform, N_{spike} is the number of samples

of each spike waveform, and V_{dc} is an arbitrary dc bias to satisfy $w_i(n) > 0, \forall i, n$.

According to the definition of EMD [60], Z in equation (21) is formulated as

$$Z(f_{uv}(t)) = \sum_{u=1}^{N_{\text{spike}}} \sum_{v=1}^{N_{\text{spike}}} d_{uv} f_{uv}(t),$$

subject to

$$\sum_{u=1}^{N_{\text{spike}}} f_{uv}(t) = w_v^{(C)}(t),$$

$$\sum_{v=1}^{N_{\text{spike}}} f_{uv}(t) = w_u^{(M)},$$

$$\sum_{u=1}^{N_{\text{spike}}} \sum_{v=1}^{N_{\text{spike}}} f_{uv}(t) = N_{\text{spike}} V_{\text{dc}},$$

$$f_{uv}(t) \geqslant 0, \qquad 1 \leqslant u \leqslant N_{\text{spike}}, \qquad 1 \leqslant v \leqslant N_{\text{spike}}.$$

Equation (21) as a linear programming problem can be considered in geometric terms as finding an optimum in a closed convex polytope. In the problem presented in this work, the polytope is defined by intersecting $2N_{\text{spike}}+1$ half-spaces in a $N_{\text{spike}} \times N_{\text{spike}}$-dimensional Euclidean space. Computing the EMD is based on a solution to the well-known transportation problem [61] from linear optimization, for which efficient algorithms, e.g., simplex methods, are available. The simplex method essentially works by searching the boundary of the polytope for an optimum. Detailed descriptions of the simplex method to solve equation (21) are presented in [62, 63]. In the experiment section, cluster isolation quality is quantitatively scored by the EMD-based similarity measure.

3.5. Comparative sorting results using synthesized spike data

Synthesized spike data from waveclus [18, 64] are used as a testing data set to compare the sorting results with both spikes and their derivatives. The data are constructed using many averaged spike shapes compiled from recordings in
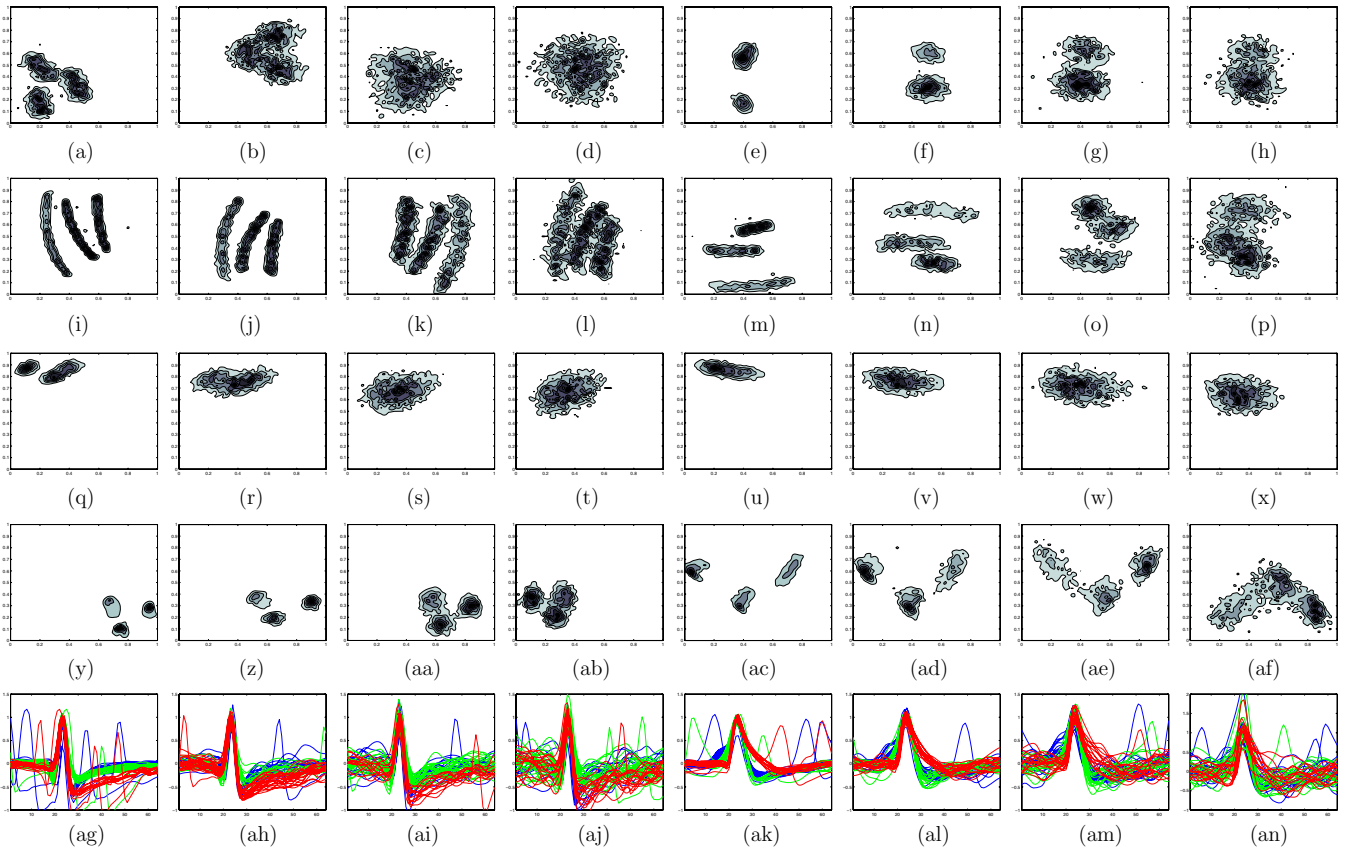
Figure 8. Feature extraction results using spikes and their derivatives. Panels (a)–(h) display the PCA-based feature extraction result using original waveforms. Panels (i)–(p) display the PCA-based feature extraction result using the derivative of spikes (proposed). Panels (q)–(x) display waveform peaks based feature extraction using original waveforms. Panels (y)–(af) display waveform peaks based feature extraction using the derivative of spikes (proposed). Panels (ag)–(an) display spike clusters used in each column. (All the algorithms are tested without performing interpolation. Overlapping spikes within 1.2 ms are ignored. Two-dimensional features are projected from a higher-dimensional space. Each column refers to a different sequence. Noise level increases from column 1 to column 4, from column 5 to column 8.)

the neocortex and basal ganglia. Simulated noise is further superimposed to the spike sequence to mimic background noise. Comparative results on challenging sequences, which contain three clusters are presented in this section.

As described in section 3.1, spikes are detected from the raw data using the NEO. ROC curves are used to quantify the performance of detection algorithms, and comparative results are plotted in figure 7.

The 'probability of correct detection' used in figure 7 is defined as the ratio of the number of correctly detected spikes over the number of total neural spikes. The 'probability of false detection' is defined as the ratio of the number of detected noise events over the number of total detected spikes. For example, if the number of neural spikes is 100 and the detector detects 120 spikes, among which 99 spikes are neural spikes and 21 events are noise, the 'probability of correct detection' is 99/100 and 'probability of false detection' is 21/120. With NEO-based spike detection, the detection threshold is set to be three times the RMS score, which corresponds to 1.4% error detection and detects 99.5% spikes as a worst case in this data set (detailed information is shown in table 2). The detected spike with an interval less than 1.2 ms is treated as overlapping events and ignored.

After detection, spikes are simply aligned according to the peaks before feature extraction. The alignment is performed without interpolation or waveform fitting. The results from the PCA-based spike feature extraction algorithm are shown in figures 8(a)–(h) and (i)–(p). In figures 8(a)–(h), features are extracted from spikes. As a comparison, features extracted from the derivative of spikes are shown in figures 8(i)–(p), where a three-cluster configuration is clearly visible. The results of using waveform peak based feature extraction algorithms are shown in figures 8(q)–(x) and (y)–(af). In figures 8(q)–(x), the features are constructed from the peaks of the spikes. Features using the peaks of spike derivative and spike height are shown in figures 8(q)–(x). Again, improved cluster isolation is observed when extracting features from the spike derivatives.

Following [17], the classification matrix is used to quantify the performance of spike sorting algorithms. It is defined as

$$
CM = \begin{vmatrix}
 & N1 & N2 & N3 \\
C1 & d_1 & r_4 & r_5 \\
C2 & r_1 & d_2 & r_6 \\
C3 & r_3 & r_2 & d_3
\end{vmatrix},
$$

where $N1$, $N2$ and $N3$ represent spikes belonging to each neuron, while $C1$, $C2$ and $C3$ represent the clusters

Table 1. Classification matrix for sorting results using the derivative of spikes.

PCA + spike derivative

#1	N1	N2	N3	#2	N1	N2	N3	#3	N1	N2	N3	#4	N1	N2	N3
C1	985	8	2		1047	10	3		1032	8	6		1005	13	26
C2	9	974	2		14	1038	4		10	1046	5		14	953	7
C3	25	22	1040		23	20	1020		25	16	1025		29	45	1053

#5	N1	N2	N3	#6	N1	N2	N3	#7	N1	N2	N3	#8	N1	N2	N3
C1	997	5	11		1088	10	14		931	53	14		863	55	51
C2	18	986	18		17	1029	13		54	931	18		122	971	20
C3	12	8	997		4	6	1022		40	7	1056		59	14	984

Waveform peaks + spike derivative

#1	N1	N2	N3	#2	N1	N2	N3	#3	N1	N2	N3	#4	N1	N2	N3
C1	982	12	7		1042	13	7		978	11	14		978	15	16
C2	8	974	2		14	1038	4		10	1045	9		13	959	20
C3	29	18	1035		28	17	1016		79	14	1012		57	37	1050

#5	N1	N2	N3	#6	N1	N2	N3	#7	N1	N2	N3	#8	N1	N2	N3
C1	998	5	14		1091	18	18		973	119	19		992	118	58
C2	16	986	14		13	1021	8		17	865	12		18	908	11
C3	13	8	998		5	6	1023		35	7	1057		34	14	986

Table 2. Spike sorting accuracy comparisons

Sequence number	1	2	3	4	5	6	7	8
Total neural spikes	3383	3448	3472	3414	3364	3462	3440	3493
Detected spikes	3382	3448	3470	3413	3361	3460	3438	3476
Noise events	0	0	0	0	0	0	2	52
Non-overlapping spikes	3067	3179	3172	3415	3052	3203	3104	3139
PCA (SA)	98%	89%	60%	55%	98%	78%	80%	69%
PCA + derivative (SA)	98%	98%	98%	96%	98%	98%	94%	90%
Spike peaks (SA)	34%	34%	35%	34%	36%	38%	36%	36%
Spike peaks + derivative (SA)	98%	97%	96%	95%	98%	98%	93%	92%

distinguished by the sorting algorithms. The ideal performance should have the sorting results perfectly matching the 'ground truth', which corresponds to $r_j = 0$, $j = 1, 2, \ldots, 6$. The sorting accuracy is defined as the ratio of the number of correctly sorted spikes over the total number of correctly detected spikes:

$$\text{SA} = \frac{\sum d_i}{\sum d_i + \sum r_j}, \qquad i = 1, 2, 3, \quad j = 1, 2, \ldots, 6.$$

(23)

Quantitative sorting results of the sequences displayed in figure 8 are summarized using classification matrices, as shown in table 1. The sorting accuracies defined by equation (23) are listed in table 2 as a performance measure to quantitatively compare the results. In those sequences, improved performance is observed by sorting the derivatives of spikes rather than the original waveforms.

EMD is applied for the quantitative evaluation of the spike waveform separation before and after derivation. To estimate the spike variations of a neuron *A*, waveforms are randomly picked from the corresponding waveform cluster *A* (here 'cluster' refers to the waveform bundle for one neuron), and the distance between them is calculated using EMD. We repeat the procedures of randomly picking waveforms and computing their distances for a different neuron *B*. The test results on eight pairs of neurons (measuring EMD 300 times

for each pair of neurons) are summarized in figure 9(a) as the black (■) dotted trace. To further estimate the waveform separation between neuron *A* and *B*, we randomly pick two waveforms, one from cluster *A* and the other from cluster *B*, and compute the EMD between them. The test results are summarized in figure 9(a) as the red (▲) dotted trace.

In figure 9(b), we apply similar procedures on the same eight pairs of candidate neurons. The only difference from tests shown in figure 9(a) is that waveform derivatives are used instead of their original counterparts. In this set of experiments, the black (■) dotted and red (▲) dotted curves represent the intra-cluster and inter-cluster distances of the eight pairs of neurons, exhibiting smaller standard deviations and improved separation. For the convenience of comparing intra-cluster and inter-cluster distances, before and after taking the derivative, waveforms are normalized to the same scale.

4. Summary and discussion

We present a technique of using the first derivative of spikes to improve the separation of recorded signals from similar neurons. To obtain a quantitative measure of the improvement in performance, synthesized spike waveforms from a public database [64] are applied as testing sequences. The NEO-based detection algorithm with specified threshold is used to detect spikes. More than 99.5% detection accuracy with
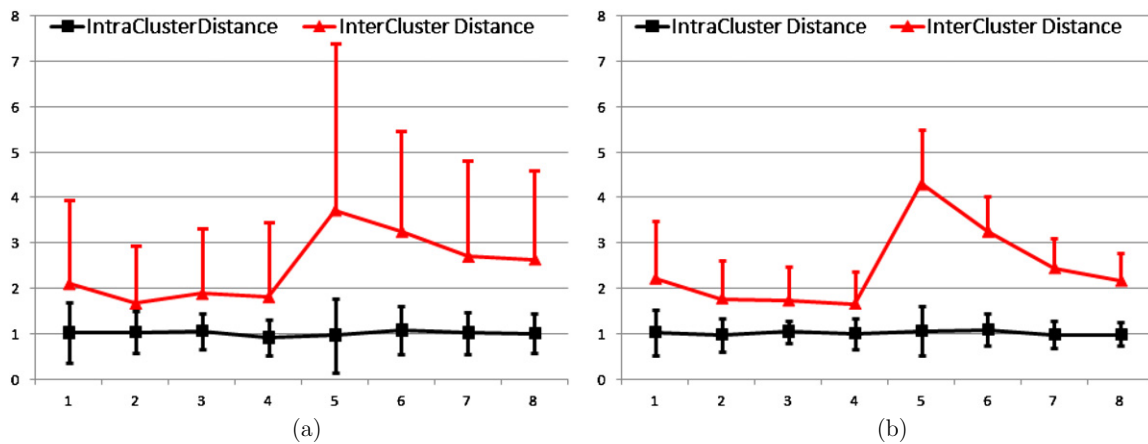
Figure 9. Quantitative evaluations of the spike waveform separation quality before and after derivative. Eight pairs of neurons are indicated by the horizontal axis. (a) Intra-cluster and inter-cluster EMDs of the original spike waveforms. (b) Intra-cluster and inter-cluster EMDs of the spike waveforms after derivative. After derivation, the standard deviations of both intra-cluster distance and inter-cluster distance noticeably reduce, suggesting improved waveform separation.

less than 1.4% false detection are observed when tested on the noisy sequence in the database. Popular feature extraction algorithms, including PCA and spike peaks are applied without using any complex training algorithms. In the feature space, cluster configuration with improved isolation quality is visualized when features are extracted from the first derivative of the waveforms. Due to uncertainties from the cluster geometry and density, an evolving mean shift clustering algorithm that performs clustering based on density gradient is, therefore, used. Classification matrices and tabulated sorting accuracy summary are presented to show a statistical representation of the sorting results, which clearly demonstrates improvement in performance when using the first derivative of waveforms.

The advantage of using the first derivative of spikes is that it emphasizes the high-frequency spectrum, which manifests the waveform difference contributed by neurons' geometry kernel function as well as the shapes noise spectrum. Given the condition of similar spike height and shape from two neurons, the spectrum of the kernel function deviates to higher frequencies. As a result, a frequency shaping filter with an emphasis on the high-frequency spectrum helps to identify different kernel functions. Two reasons are responsible for using the first derivative as the default frequency shaping filter. First, the small computation requirement of the algorithm enables an integrated microchip implementation as shown in [65–67]. Second, taking the first derivative reduces the total noise when evaluated with real recorded noise waveforms from different preparations. A frequency shaping filter with an emphasis on a high-frequency spectrum magnifies high-frequency noise, which may degenerate the waveform separation if over emphasized.

In summary, our test results show appreciable sorting improvement by using the first derivative of spikes. However, it is not necessary the 'optimal' frequency shaping filter. The optimal filter is clearly related to the noise profile, which varies according to the recording system and biological environment. As a result, an 'optimal' frequency shaping filter may involve additional training and calibration.

Acknowledgments

References

[1] Lewicki M S 1998 A review of methods for spike sorting: the detection and classification of neural action potentials *Net. Comput. Neural. Syst.* **9** 53–78

[2] Rutishauser U, Schuman E M and Mamelak A N 2006 Online detection and sorting of extracellularly recorded action potentials in human medial temporal lobe recordings, *in vivo J. Neurosci. Methods* **154** 204–24

[3] Wood F, Black M J, Vargas-Irwin C, Fellows M and Donoghue J P 2004 On the variability of manual spike sorting *IEEE Trans. Biomed. Eng.* **51** 912–8

[4] Chapin J K 2004 Using multi-neuron population recordings for neural prosthetics *Nat. Neurosci.* **7** 452–5

[5] Serruya M D, Hatsopoulos N G, Paninski L, Fellows M R and Donoghue J P 2002 Instant neural control of a movement signal *Nature* **416** 141–2

[6] Hochberg L R *et al* 2006 Neuronal ensemble control of prosthetic devices by a human with tetraplegia *Nature* **442** 164–71

[7] Quirk M C, Blum K I and Wilson M A 2001 Experience-dependent changes in extracellular spike amplitude may reflect regulation of dendritic action potential back-propagation in rat hippocampal pyramidal cells *J. Neurosci.* **21** 240–8

[8] Kaneko H, Tamura H and Suzuki S S 2007 Tracking spike-amplitude changes to improve the quality of multineuronal data analysis *IEEE Trans. Biomed. Eng.* **54** 262–72

[9] Bar-Hillel A, Spiro A and Stark E 2006 Spike sorting: Bayesian clustering of non-stationary data *J. Neurosci.* **157** 303–16

[10] Zumsteg Z S *et al* 2005 Power feasibility of implantable digital spike sorting circuits for neural prosthetic systems *IEEE Trans. Neural. Syst. Rehabil. Eng.* **13** 272–9

[11] Thakur P H, Lu H, Hsiao S S and Johnson K O 2007 Automated optimal detection and classification of neural action potentials in extra-cellular recordings *J. Neurosci. Methods* **162** 364–76

[12] Lewicki M S 1994 Bayesian modeling and classification of neural signals *Adv. Neural. Inf. Process. Syst.* **6** 590–7

[13] Vargas-Irwin C and Donoghue J P 2007 Automated spike sorting using density grid contour clustering and subtractive waveform decomposition *J. Neurosci. Methods* **164** 1–18

[14] Lewicki M S 1994 Bayesian modeling and classification of neural signals *Neural. Comput.* **6** 1005–30

[15] Vollgraf R and Obermayer K 2006 Improved optimal linear filters for the discrimination of multichannel waveform templates for spike-sorting applications *IEEE Signal Process. Lett.* **13** 121–4

[16] Zhang P, Wu J, Zhou Y, Liang P and Yuan J 2004 Spike sorting based on automatic template reconstruction with a partial solution to the overlapping problem *J. Neurosci. Methods* **7** 446–51

[17] Letelier J C and Weber P P 2000 Spike sorting based on discrete wavelet transform coefficients *J. Neurosci. Methods* **101** 93–106

[18] Quian Quiroga R, Nadasdy Z and Ben-Shaul Y 2004 Unsupervised spike detection and sorting with wavelets and superparamagnetic clustering *Neural. Comput.* **16** 1661–87

[19] Pavlov A, Makarov V A, Makarova I and Panetsos F 2007 Sorting of neural spikes: when wavelet based methods outperform principal component analysis *Natural Comput.* **6** 269–81

[20] Takahashi S and Sakurai Y 2007 Coding of spatial information by soma and dendrite of pyramidal cells in the hippocampal CA1 of behaving rats *Eur. J. Neurosci. Methods* **26** 2033–45

[21] Sakurai Y, Tamura H and Takahashi S 2006 Dynamic synchrony of firing in the monkey prefrontal cortex during working-memory tasks *J. Neurosci.* **26** 10141–53

[22] Snellings A, Anderson D and Aldridge J 2006 Improved signal and reduced noise in neural recordings from close-spaced electrode arrays using independent component analysis as a preprocessor *J. Neurosci. Methods* **150** 254–64

[23] Takahashi S and Sakurai Y 2005 Real-time and automatic sorting of multi-neuronal activity for sub-millisecond interactions *in vivo Neuroscience* **134** 301–15

[24] Mamlouk A M, Sharp H, Menne K M L, Hofmann U G and Martinetz T 2005 Unsupervised spike sorting with ICA and its evaluation using GENESIS simulations *Neurocomputing* **65–6** 275–82

[25] Delescluse M and Pouzat C 2006 Efficient spike-sorting of multi-state neurons using inter-spike intervals information *J. Neurosci. Methods* **150** 16–29

[26] Liu X, McCreery D B, Bullara L A and Agnew W F 2006 Evaluation of the stability of intracortical microelectrode arrays *IEEE Trans. Neural. Syst. Rehabil. Eng.* **14** 91–100

[27] Liu X, McCreery D B, Carter R R, Bullara L A, Yuen TGH and Agnew W F 1999 Stability of the interface between neural tissue and chronicallyimplanted intracortical microelectrodes *IEEE Trans. Neural. Syst. Rehabil. Eng.* **7** 315–26

[28] Jung H K, Choi J H and Kim T 2006 Solving alignment problems in neural spike sorting using frequency domain PCA *Neurocomputing* **69** 975–8

[29] Blanche T J and Swindale N V 2006 Nyquist interpolation improves neuron yield in multiunit recordings *J. Neurosci. Methods* **155** 207–16

[30] Sahani M 1999 Latent variable models for neural data analysis *PhD Dissertation* California Institute of Technology

[31] Shenoy K V *et al* 2006 Increasing the performance of cortically-controlled prostheses *Proc. 28th Ann. Int. Conf. IEEE EMBS* pp 6652–6

[32] Linderman M D *et al* 2006 Neural recording stability of chronic electrode *Proc. 28th Ann. Int. Conf. IEEE. EMBS* pp 4387–91

[33] Holt G R and Koch C 1999 Electrical interactions via the extracellular potential near cell bodies *J. Comput. Neurosci.* **6** 169–84

[34] Buzsaki G, Penttonen M, Nadasdy Z and Bragin A 1996 Pattern and inhibition-dependent invasion of pyramidal cell dendrites by fast spikes in the hippocampus *in vivo Proc. Natl Acad. Sci. USA* **93** 9921–5

[35] Tuckwell H C 1988 *Introduction to Theoretical Neurobiology* (Cambridge: Cambridge University Press)

[36] Traub R D, Wong R K S, Miles R and Michelson H 1991 A model of a CA3 hippocampal neuron incorporating voltage-clamp data on intrinsic conductances *J. Neurophysiol.* **66** 635–50

[37] Greenberg R J, Velte T J, Humanyun M S, Scarlatis G N and De Juan E J 1999 A computational model of electrical stimulation of the retinal ganglion cell *IEEE Trans. Biomed. Eng.* **46** 505–14

[38] Rattay F, Lutter P and Felix H 2001 A model of the electrically excited human cochlear neuron I. Contribution of neural substructures to the generation and propagation of spikes *Hear. Res.* **153** 43–63

[39] Buzsaki G 2004 Large-scale recording of neuronal ensembles *Nat. Neurosci.* **7** 446–51

[40] Thurbon D, Field A and Redman S 1994 Electrotonic profiles of interneurons in stratum paramidale of the CA1 region of rat hippocampus *J. Neurophysiol.* **71** 1948–58

[41] Lewis D A 2000 GABAergic local circuit neurons and prefrontal cortical dysfunction in schizophrenia *Brain Res. Rev.* **31** 270–6

[42] Hausser M, Spruston N and Stuart G 2000 Diversity and dynamics of dendritic signaling *Science* **290** 739–44

[43] Gilja V *et al* 2006 Multiday electrophysiological recordings from freely behaving primates *Proc. 28th Ann. Int. Conf. IEEE EMBS* pp 4387–91

[44] Yang Z, Chen T and Liu W 2008 A neuron signature based spike feature extraction algorithm for on-chip implementation *Proc. 30th Ann. Int. Conf. IEEE EMBS* pp 4237–40

[45] Yang Z, Zhao Q and Liu W 2009 Spike feature extraction using informative samples *Adv. Neural. Inf. Process. Syst.* **21** 1865–72

[46] Kaiser J F 1990 On a simple algorithm to calculate the energy of a signal *Proc. IEEE Int. Conf. Acoustic. Speech and Signal Processing* pp 381–4

[47] Maragos P, Kaiser J F and Quatieri T F 1993 On amplitude and frequency demodulation using energy operators *IEEE Trans. Signal Process.* **41** 1532–50

[48] Kim K H and Kim J K 2000 Neural spike sorting under nearly 0-dB signal-to-noise ratio using nonlinear energy operator and artificial neural-network classifier *IEEE Trans. Biomed. Eng.* **47** 1406–11

[49] Gibson S, Judy J W and Markovic D 2008 Comparison of spike-sorting algorithms for future hardware implementation *Proc. 30th Ann. Int. Conf. IEEE EMBS* pp 4237–40

[50] Simon W 1965 The real-time sorting of neuro-electric action potentials in multiple unit studies *Electroencephalogr. Clin. Neurophysiol.* **18** 192–5

[51] Yang Z, Zhao Q and Liu W 2009 Energy based evolving mean shift algorithm for neural spike classification *Proc. 31th Ann. Int. Conf. IEEE EMBS (Sept)*

[52] Fukunaga K and Hostetler L D 1975 The estimation of the gradient of a density function, with application in pattern recognition *IEEE Trans. Inf. Theory* **21** 180–7

[53] Cheng Y Z 1995 Mean shift, mode seeking, and clustering *IEEE Trans. Pattern Anal. Mach. Intell.* **17** 790–9

[54] Comaniciu D and Meer P 2002 Mean shift: a robust approach toward feature space analysis *IEEE Trans. Pattern Anal. Mach. Intell.* **24** 603–19

[55] Hall P, Hui T C and Marron J C 1995 Improved variable window kernel estimates of probability densities *Ann. Stat.* **23** 1–10

[56] Swain M and Ballard D 1991 Color indexing *Int. J. Comput. Vis.* **7** 11–32

[57] Puzicha J, Hofmann T and Buhmann J M 1997 Non-parametric similarity measures for unsupervised texture segmentation and image retrieval *IEEE Conf. Comput. Vision and Pattern Recognition* pp 267–72

[58] Niblack W *et al* 1993 Querying images by content, using color, texture, and shape *SPIE Conf. Storage and Retrieval for Image and Video Databases* pp 1908, 173–87

[59] Werman M, Peleg S and Rosenfeld A 1985 A distance metric for multi-dimensional histograms *Comput. Vis. Graph. Image Process.* **32** 328–36

[60] Rubner Y 1999 Perceptual metrics for image database navigation *PhD Dissertation* Stanford University

[61] Hitchcock F 1941 The distribution of a product from several sources to numerous localities *J. Math. Phys.* **20** 224–30

[62] Hillier F S and Lieberman G J 1990 *Introduction to Mathematical Programming* (New York: McGraw-Hill)

[63] Winston W L, M V and Goldberg J B 2003 *Introduction to Mathematical Programming: Operations Research* 4th edn (Pacific Grove, CA: Duxbury)

[64] Quiroga R http://www2.le.ac.uk/departments/engineering/ research/bioengineering/neuroengineering-lab

[65] Chae M *et al* 2008 A 128 channel 6mW wireless neural recording IC with on-the-fly spike sorting and UWB transmitter *IEEE ISSCC 2008 Dig. Tech. Papers (Feb.)* vol 7 pp 241–61

[66] Chen T, Yang Z, Liu W and Chen L 2008 NEUSORT2.0: a multiple-channel neural signal processor with systolic array buffer and channel-interleaving processing schedule *Proc. 30th Ann. Int. Conf. IEEE EMBS* pp 5029–32

[67] Chen T, Chen K, Yang Z, Cockerham K and Liu W 2009 A biomedical multiprocessor SoC for closed-loop neuroprosthetic applications *IEEE ISSCC 2009 Dig. Tech. Papers (Feb.)*